THE EUROPEAN
PHYSICAL JOURNAL C

Search for high-frequency gravitational waves with Rydberg atoms

Sugumi Kanno[1] , **Jiro Soda**[2,3] , **Akira Taniguchi**[1,a]

[1] Department of Physics, Kyushu University, Fukuoka 819-0395, Japan
[2] Department of Physics, Kobe University, Kobe 657-8501, Japan
[3] International Center for Quantum-field Measurement Systems for Studies of the Universe and Particles (QUP), KEK, Tsukuba 305-0801, Japan

Abstract   We propose high-frequency gravitational wave (GW) detectors with Rydberg atoms. Rydberg atoms are ultra-sensitive detectors of electric fields. By setting up a constant magnetic field, a weak electric field is generated upon the arrival of GWs. The weak electric field signal is then detected by an electromagnetically induced transparency (EIT) in the system of the Rydberg atoms. Recently, the minimum detectable electric field with the Rydberg atoms is further improved by employing superheterodyne detection method. Hence, even the weak signal generated by GWs turns out to be detectable. We calculate the amplitude of Rabi frequency of the Rydberg atoms induced by the GWs and show that the sensitivity of the Rydberg atoms becomes maximum when the size of the Rydberg atoms is close to the wavelength of GWs. We evaluate the minimum detectable amplitude of GWs with Rubidium Rydberg atoms and find that the detector can probe GWs with a frequency $f = 4.2$ GHz and an amplitude around 10^{-20}.

Contents

1 Introduction

The discovery of gravitational waves (GWs) from a merging black hole binary by LIGO-Virgo Collaboration [1] triggered a new field of science, so-called GW astronomy. As the history of astronomy tells us, it would be crucial to expand the range of observable GW frequency for making further discoveries. Currently, LIGO/Virgo/KAGRA are sensitive to GWs with frequencies only in the range of $10 \sim 10^2$ Hz [2]. The future space-based GW observatories such as LISA [3] and DECIGO [4,5] will cover the low-frequency band $10^{-4} \sim 10^{-1}$ Hz. Moreover, Pulsar timing arrays are expected to operate in the lower-frequency band $10^{-9} \sim 10^{-7}$ Hz. Recently, it has been reported that the pulsar timing arrays have successfully observed GWs [6–14]. Thus, GWs in the frequency range from 10^{-9} to 10^2 Hz have been well explored.

On the other hand, observations of GWs at frequencies higher than 10 kHz have not been well developed. This is partially due to a tacit assumption that GWs with a frequency higher than 10 kHz have no relevance to physics. However, the high-frequency GWs associated with astrophysical phenomena could exist [15,16]. Moreover, primordial black holes (PBHs) lighter than solar mass can produce GWs with frequencies higher than 10 kHz. We can also expect high-frequency GWs from inflation [17,18]. The frequency of primordial GWs generated by reheating is typically in the range

from MHz to GHz [18]. High-frequency GWs could be generated by cosmological events even after inflation such as the cosmological phase transitions in the early universe [19]. In addition, we consider GWs from extra dimensions as the possible candidates for GW sources that could lead to verifying theories beyond the Standard Model. According to [20], GWs generated by pointlike bodies orbiting a braneworld black hole can produce observable high-frequency GWs. Hence, observations of high-frequency GW will provide information beyond the Standard Model of particle physics (see a review article [21]).

Another reason why GWs with frequencies higher than 10 kHz have not been explored is the presence of obstacles in their detection. Indeed, it is known that the sensitivity of current GW detectors becomes worse in the high-frequency range [22]. Hence, it is necessary to come up with new schemes for the detection of GWs at frequencies above 10 kHz. A hint can be obtained by focusing on the similarities between axions and GWs. That is, if axions can be detected, it opens the possibility of detecting GWs as well. Based on this idea, the use of axion detection with magnons provided constraints on high-frequency GWs [23,24]. This approach can be applied to the interaction between axions and various other excitations, such as axion-photon conversion [25,26]. Recently, an idea for the detection of axion by using Rydberg atoms was proposed in [27]. Following the strategy mentioned above, we focus on the similarities between axions and GWs, and then see if we can exploit the Rydberg atoms for detecting high-frequency GWs.

Since Rydberg atoms can exhibit very large electric dipole moments [28], they are widely used to measure electric fields as quantum sensors [29]. Indeed, it is possible to measure microwave electric fields over a wide range of frequencies from kHz [30] to THz [31,32]. The Rydberg atoms can be used as GW detectors because GWs induce a weak electric field when propagating in a homogeneous constant magnetic field. Recently, highly sensitive detection utilizing electromagnetically induced transparency (EIT) with an atomic superheterodyne receiver has been developed [33]. Therefore, it would be worth investigating the possibility of detecting high-frequency GWs with the Rydberg atoms.[1] In particular, the detector with Rydberg atoms has a potential for utilizing quantum entanglement to realize Heisenberg scaling.

The paper is organized as follows. In Sect. 2, we explain our strategy for detecting GWs based on the fact that the electric field can be induced by GWs in the presence of a magnetic field. In Sect. 3, we start with basics of Rabi oscillations. We derive the relation between the susceptibility and density matrix of Rydberg atoms. Then, by solving the mas-

ter equation, we explain a mechanism of EIT. In Sect. 4, we review the basic idea of Rydberg atom superheterodyne receiver and describe how to use it as a GW detector. Moreover, we review the full-order Fermi normal coordinates for plane GWs. In Sect. 5, we deduce the density matrix by solving the Lindblad master equation for the system of Rydberg atom. Then, we evaluate the sensitivity of GW detectors with Rydberg atom. We also discuss the possibility of Heisenberg scaling to enhance the sensitivity. The final section is devoted to conclusion. In appendix, the details of calculations for the averaged amplitude of GW are presented. We work in natural unit: $\hbar = c = \varepsilon_0 = \mu_0 = 1$.

2 A strategy for detecting GWs

In this section, we propose a method for detecting high-frequency GWs. In the presence of a uniform magnetic field, GWs induce electric fields. The idea is to detect the electric fields by a heterodyne detection method with Rydberg atoms [33].

We first derive the electric field induced by GWs. Below we work in the laboratory frame. We consider a situation where GWs propagate in a constant magnetic field. The action we consider is the electromagnetic fields expressed by

$$S = \int d^4x \sqrt{-g} \left[-\frac{1}{4} F^{\mu\nu} F_{\mu\nu} \right]. \tag{2.1}$$

We consider the tensor mode perturbation $h_{\mu\nu}$ in the four-dimensional metric:

$$ds^2 = (\eta_{\mu\nu} + h_{\mu\nu}) dx^\mu dx^\nu \tag{2.2}$$

where $\eta_{\mu\nu} = \mathrm{diag}(-1, 1, 1, 1)$ represents the Minkowski metric. The indices (μ, ν) run from 0 to 3, and $(0, 1, 2, 3) = (t, x, y, z)$. Substituting Eq. (2.2) into the action (2.1), the action up to the first order in $h_{\mu\nu}$ is given by

$$S = \int d^4x \left[-\frac{1}{4} F^{\mu\nu} F_{\mu\nu} - \frac{1}{4} \left(\frac{1}{2} h F^{\mu\nu} F_{\mu\nu} \right. \right.$$
$$\left. \left. + h^\nu{}_\alpha F^{\alpha\mu} F_{\mu\nu} - h^\mu{}_\alpha F^{\alpha\nu} F_{\mu\nu} \right) \right] \tag{2.3}$$

where $F^{\mu\nu} = \partial^\mu A^\nu - \partial^\nu A^\mu$ is the field strength of a gauge field A^μ. The variation of the action (2.3) with respect to the gauge field A^μ gives the Maxwell equation,

$$\partial_\nu F^{\mu\nu} + \partial_\nu \left(\frac{1}{2} h F^{\mu\nu} + h^\nu{}_\alpha F^{\alpha\mu} - h^\mu{}_\alpha F^{\alpha\nu} \right) = 0. \tag{2.4}$$

---

[1] See the literature [34] that considers Rydberg atoms to detect 100 Hz GWs as an earlier work.

If we consider the situation that the electric field E^i is induced by the interaction between the constant magnetic field B^i and GWs, then $B^i \sim \mathcal{O}(1)$ and $E^i \sim \mathcal{O}(h)$. Equation (2.4) at the first order in h becomes

$$\partial_i \left(E^i - h^0{}_j \varepsilon^{jik} B^k \right) = 0 \tag{2.5}$$

where we used the relations $F^{0i} = E^i$ and $F^{ij} = \varepsilon^{ijk} B^k$. This can be integrated as

$$E^i - h^0{}_j \varepsilon^{jik} B^k = \varepsilon^{ijk} \partial_j C^k, \tag{2.6}$$

where C^k is an arbitrary constant function. If we impose the initial condition that no electric field is induced without the magnetic field, then $C^i = 0$. Thus, we obtain

$$E^i = \varepsilon^{ijk} h^0{}_j B^k. \tag{2.7}$$

We can naively guess that the magnitude of the induced electric fields is of the order of

$$E^i = 10^{-17} \left(\frac{h}{10^{-20}} \right) \left(\frac{B}{10\,\mathrm{T}} \right) \mathrm{eV}^2$$
$$\sim 10^{-13} \left(\frac{h}{10^{-20}} \right) \left(\frac{B}{10\mathrm{T}} \right) \mathrm{V/cm}. \tag{2.8}$$

Our goal is to study the details of the detection method and clarify if we can detect this tiny electric fields with Rydberg atoms.

3 Measurement of electric field with EIT

In the previous section, we showed the strategy for detecting gravitational waves by measuring the electric field. In this section, we review the concept of Electromagnetically induced transparency (EIT) in quantum optics that can be used to measure electric field signals [35].

3.1 Interaction of a two-level atom with an electric field

We first review the interaction system between two-level atoms and the probe laser. Let us consider a situation where the two-level atom with energies ε_1 and ε_2 interacts with an electric field (probe laser) $\boldsymbol{E}_p \cos(\omega_p t)$ as shown in Fig. 1a. The total Hamiltonian for this system can be written as

$$\hat{H} = \hat{H}_0 + \hat{H}'(t) \tag{3.1}$$

where $\hat{H}_0$ represents an unperturbed Hamiltonian and $\hat{H}'(t)$ represents an interaction Hamiltonian. They are written as

$$\hat{H}_0 = \varepsilon_1 |1\rangle \langle 1| + \varepsilon_2 |2\rangle \langle 2| \tag{3.2}$$
$$\hat{H}'(t) = -\hat{\boldsymbol{d}} \cdot \boldsymbol{E}_p \cos(\omega_p t) \tag{3.3}$$

where $\hat{\boldsymbol{d}} \equiv e\hat{\boldsymbol{r}}$ is the electric dipole moment operator and is expressed as

$$\hat{\boldsymbol{d}} = \boldsymbol{d}_{12} |1\rangle \langle 2| + \boldsymbol{d}_{21} |2\rangle \langle 1|. \tag{3.4}$$

Here $\boldsymbol{d}_{12} = \langle 1| e\hat{\boldsymbol{r}} |2\rangle$ and $\boldsymbol{d}_{21} = \langle 2| e\hat{\boldsymbol{r}} |1\rangle$. Note that $\boldsymbol{d}_{ij}$ represent the electric dipole moment associated with the transition from $|i\rangle$ to $|j\rangle$. Thus, we can write the interaction Hamiltonian as follows:

$$\hat{H}'(t) = -\hat{\boldsymbol{d}} \cdot \boldsymbol{E}_p \cos(\omega_p t)$$
$$= -\frac{1}{2} \left(\boldsymbol{d}_{12} \cdot \boldsymbol{E}_p |1\rangle \langle 2| + \boldsymbol{d}_{21} \cdot \boldsymbol{E}_p |2\rangle \langle 1| \right)$$
$$\times \left(e^{i\omega_p t} + e^{-i\omega_p t} \right)$$
$$= -\frac{\Omega_p}{2} e^{-i\omega_p t} |2\rangle \langle 1| - \frac{\Omega_p}{2} e^{i\omega_p t} |1\rangle \langle 2| \tag{3.5}$$

where we used the rotation wave approximation, namely, the terms $e^{-i\omega_p t} |1\rangle \langle 2|$ and $e^{i\omega_p t} |2\rangle \langle 1|$ are ignored. This is because $e^{-i\omega_p t} |1\rangle \langle 2|$ represents a transition in which a photon is absorbed and the energy level drops from $|2\rangle$ to $|1\rangle$, and $e^{i\omega_p t} |2\rangle \langle 1|$ represents a transition in which a photon is emitted and the energy level goes up from $|1\rangle$ to $|2\rangle$, which are physically suppressed.

We note that the transition from $|1\rangle$ to $|2\rangle$ can be realized by absorbing the probe laser with the frequency corresponding to the energy gap of the two levels $\varepsilon_2 - \varepsilon_1$. The probe laser $\boldsymbol{E}_p \cos(\omega_p t)$ can induce the Rabi oscillation with the Rabi frequency $\Omega_p \equiv |\boldsymbol{d}_{12} \cdot \boldsymbol{E}_p|$. In this two-level system, the atoms absorb the probe laser in the resonance condition $\Delta_p = 0$ as shown in Fig. 1b.

3.2 Susceptibility and density matrix

In this subsection, we show that the absorption rate of the probe laser and the density operator of the system are related through the complex susceptibility. Specifically, it is known that the absorption rate is proportional to the imaginary part of electric susceptibility which can be related to the density operator of an atom.
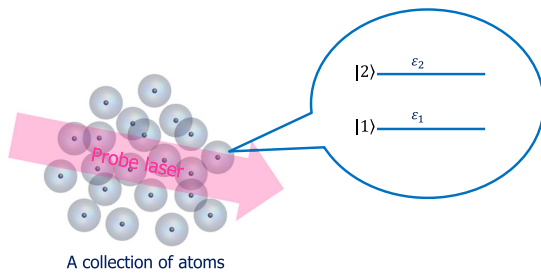
First, we show that the absorption rate is proportional to the imaginary part of electric susceptibility. Let us consider the electric field of a plane electromagnetic wave traveling in the z-direction

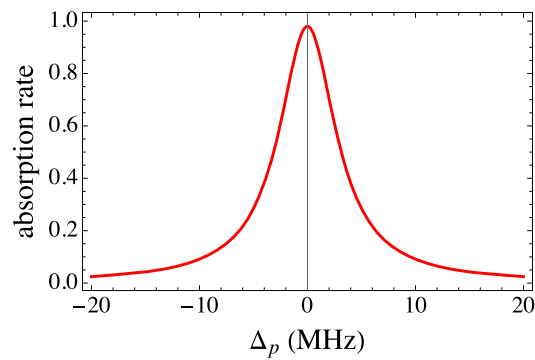$$E(z, t) = E_0 \exp(ikz - i\omega t), \tag{3.6}$$

where E_0 is the amplitude of the electric field. The complex relative permittivity $\varepsilon(\omega, k)$ is expressed as

$$\varepsilon(\omega, k) = 1 + \chi(\omega, k) \tag{3.7}$$

where $\chi(\omega, k)$ ($|\chi| \ll 1$) is the linear susceptibility. We can introduce the refractive index $n(\omega)$ and the extinction coefficient $\kappa(\omega)$ by separating $\sqrt{\varepsilon(k, \omega)}$ into its real and imaginary parts such as

(a) Sketch of the spectroscopic setup.

(b) The absorption rate of the probe laser.

Fig. 1 (**a**) The spectroscopic setup where probe laser is directed at the collection of two-level Rydberg atoms. (**b**) The absorption rate of the probe laser as a function of the detuning Δ_p. The probe laser is shown to be absorbed by the atoms as Δ_p goes to zero

$$\sqrt{\varepsilon(k,\omega)} = \frac{k}{\omega} \equiv n(\omega) + i\kappa(\omega). \tag{3.8}$$

Then Eq. (3.6) is written as

$$E(z,t) = E_0 \exp\left[i\left(\omega n(\omega)z - \omega t\right)\right] \exp\left[-\omega\kappa(\omega)z\right]. \tag{3.9}$$

Note that $\kappa(\omega)$ represents an exponential decay of the electric field, so it is referred to as absorption rate. Next, defining real and imaginary parts of the susceptibility as χ' and χ'', we can write

$$\chi \equiv \chi' + i\chi''. \tag{3.10}$$

Substituting Eq. (3.10) into Eqs. (3.7) and (3.8), we find

$$\kappa(\omega) = \frac{\chi''}{2}. \tag{3.11}$$

This shows that the absorption rate is proportional to the imaginary part of susceptibility.

Next, we derive the relation between the susceptibility and density matrix of an atom. Let us focus on a two-level system $|1\rangle$ and $|2\rangle$ of an atom. In the semiclassical theory, the polarization $\boldsymbol{P}$ at the position of an atom induced by the probe laser $E_p \cos(\omega_p t)$ is expressed as $\boldsymbol{P}(t) = N\text{Tr}[\hat{\boldsymbol{d}}\rho(t)]$, where N is the atom number density and $\rho(t)$ is the density operator of the atom. Combining this with Eq. (3.4), we have

$$\boldsymbol{P}(t) = N\boldsymbol{d}_{12}\rho_{21}(t) + \text{ c.c.}. \tag{3.12}$$

If we decompose the polarization $\boldsymbol{P}(t)$ into Fourier modes, we have

$$\boldsymbol{P}(t) = \tilde{\boldsymbol{P}}(\omega_p)e^{-i\omega_p t} + \text{ c.c.}. \tag{3.13}$$

where $\tilde{\boldsymbol{P}}(\omega_p)$ is the Fourier transform of $\boldsymbol{P}(t)$. By comparing Eq. (3.12) with Eq. (3.13), we find

$$\tilde{\boldsymbol{P}}(\omega_p) = N\boldsymbol{d}_{12}\rho_{21}(t)e^{i\omega_p t}. \tag{3.14}$$

Similarly, the electric field $\boldsymbol{E}(t) = E_p \cos(\omega_p t)$ is decomposed into Fourier mode

$$\boldsymbol{E}(t) = \tilde{\boldsymbol{E}}(\omega_p)e^{-i\omega_p t} + \text{c.c.} = \frac{1}{2}\boldsymbol{E}_p e^{-i\omega_p t} + \text{c.c.} \tag{3.15}$$

with $\tilde{\boldsymbol{E}}(\omega_p)$ being the Fourier transform of $\boldsymbol{E}(t)$. Note that we used $\cos(\omega_p t) = \left(e^{i\omega_p t} + e^{-i\omega_p t}\right)/2$ in the second equality. The susceptibility is defined by

$$\tilde{\boldsymbol{P}}(\omega_p) = \chi(\omega_p)\tilde{\boldsymbol{E}}(\omega_p). \tag{3.16}$$

So if we use Eqs. (3.14), (3.15) and (3.16), the susceptibility is found to be related to the density operator of the atom

$$\chi(\omega_p) = \frac{2N|\boldsymbol{d}_{12}|^2}{\Omega_p}\rho_{21}(t)e^{i\omega_p t}. \tag{3.17}$$

From the above equations Eqs. (3.11) and (3.17), we can see that the absorption rate can be evaluated from the density operator. Therefore, in the next step, we present a specific system and find its density operator.
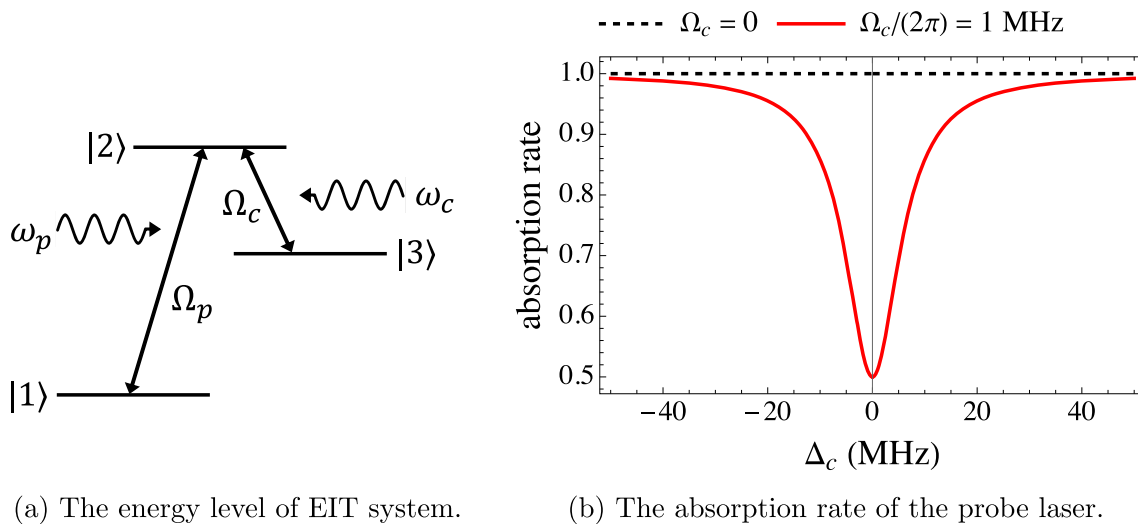
3.3 Electromagnetically induced transparency (EIT)

In this subsection, we consider the interaction of a three-level system with two electric fields as shown in Fig. 2a and show the EIT is induced. The probe laser with a frequency ω_p couples $|1\rangle$ and $|2\rangle$ with the Rabi frequency Ω_p. The control laser with a frequency ω_c couples $|2\rangle$ and $|3\rangle$ with the Rabi frequency Ω_c. The goal of this subsection is to calculate the density operator for this system and clarify the characteristics of the absorption rate of the probe laser.

The Hamiltonian for this total system is written as

$$\hat{H}(t) = \hat{H}_0 + \hat{H}'(t) \tag{3.18}$$

with the unperturbed Hamiltonian

$$\hat{H}_0 = \varepsilon_1 |1\rangle\langle 1| + \varepsilon_2 |2\rangle\langle 2| + \varepsilon_3 |3\rangle\langle 3| \tag{3.19}$$

(a) The energy level of EIT system.

(b) The absorption rate of the probe laser.

Fig. 2 (**a**) The energy level of EIT system. The probe laser with a frequency ω_p couples $|1\rangle$ and $|2\rangle$ with a Rabi frequency Ω_p, and the control laser with a frequency ω_c couples $|2\rangle$ and $|3\rangle$ with a Rabi frequency Ω_c. (**b**) Plots of the absorption rate of the probe laser. For sim-
plicity, the parameters are set to $\gamma_2/(2\pi) = \gamma_3/(2\pi) = 0.1$ MHz, $\Omega_p/(2\pi) = 1$ MHz and the resonance condition $\Delta_p = 0$ is assumed. The absorption rate is defined as $\Im\chi/(\Im\chi)_{\text{max}}$

where ε_i with $i = 1, 2, 3$ denotes the energy of each level. The dipole interaction Hamiltonian reads

$$\hat{H}'(t) = -\frac{\Omega_p}{2}e^{-i\omega_p t}|2\rangle\langle 1| - \frac{\Omega_c}{2}e^{-i\omega_c t}|3\rangle\langle 2| + \text{h.c.}$$
(3.20)

where Ω_p and Ω_c are Rabi frequencies. It is convenient to transform the Hamiltonian to a rotating frame by using

$$\hat{\mathcal{H}} = \hat{U}\hat{H}\hat{U}^\dagger - i\hat{U}\frac{d}{dt}\hat{U}^\dagger$$
(3.21)

with the unitary operator

$$\hat{U} \equiv \exp\left[i\varepsilon_1|1\rangle\langle 1|t + i(\varepsilon_1 + \omega_p)|2\rangle\langle 2|t\right.$$
$$\left. + i(\varepsilon_1 + \omega_p - \omega_c)|3\rangle\langle 3|t\right].$$
(3.22)

Then, the Hamiltonian in the rotating frame is written by

$$\hat{\mathcal{H}} = \Delta_p|2\rangle\langle 2| + (\Delta_p + \Delta_c)|3\rangle\langle 3|$$
$$+ \left[-\frac{\Omega_p}{2}|2\rangle\langle 1| - \frac{\Omega_c}{2}|2\rangle\langle 3| + \text{h.c.}\right]$$
(3.23)

where we defined detunings Δ_p and Δ_c expressed by

$$\Delta_p \equiv (\varepsilon_2 - \varepsilon_1) - \omega_p$$
(3.24)
$$\Delta_c \equiv (\varepsilon_2 - \varepsilon_3) - \omega_c.$$
(3.25)

The master equation for the density matrix of the total system in the rotating frame $\tilde{\rho}$ is given by

$$\frac{d}{dt}\tilde{\rho} = -i[\hat{\mathcal{H}}, \tilde{\rho}] + \sum_{k=2,3}\gamma_k\left[\hat{O}_k\tilde{\rho}\hat{O}_k^\dagger - \frac{1}{2}\left\{\hat{O}_k^\dagger\hat{O}_k, \tilde{\rho}\right\}\right].$$
(3.26)

where $\hat{O}_k = |1\rangle\langle k|$ represents the relaxation process of the atom. We assume that the atom is in the ground state ini-
tially, that is, the initial condition becomes $\tilde{\rho}_{11}(0) = 1$, $\tilde{\rho}_{12}(0) = \tilde{\rho}_{13}(0) = \tilde{\rho}_{22}(0) = \tilde{\rho}_{23}(0) = \tilde{\rho}_{33}(0) = 0$. In order to solve the master equation (3.26), we use linear approximation under the assumption that the frequency of the Rabi oscillation Ω_p is small enough. Under this assumption, we can assume $\tilde{\rho}_{11} = \Omega_c = \mathcal{O}(1)$, $\tilde{\rho}_{12} = \tilde{\rho}_{13} = \tilde{\rho}_{22} = \tilde{\rho}_{23} = \mathcal{O}(\Omega_p)$. Thus, the master equations become
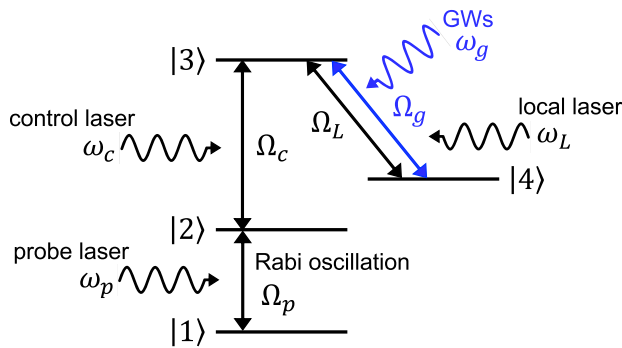
$$\frac{d}{dt}\tilde{\rho}_{21} = -\left(\frac{\gamma_2}{2} + i\Delta_p\right)\tilde{\rho}_{21} + i\frac{\Omega_p}{2}\tilde{\rho}_{11} + i\frac{\Omega_c}{2}\tilde{\rho}_{31} \quad (3.27)$$
$$\frac{d}{dt}\tilde{\rho}_{31} = -\left(\frac{\gamma_3}{2} + i(\Delta_p - \Delta_c)\right)\tilde{\rho}_{31} + i\frac{\Omega_c}{2}\tilde{\rho}_{21}. \quad (3.28)$$

Now, we obtain the stationary state solution $\tilde{\rho}_{21}^{\text{st}}$ normalized by $\tilde{\rho}_{11}$ as

$$\frac{\tilde{\rho}_{21}^{\text{st}}}{\tilde{\rho}_{11}} = \frac{i\left[\gamma_3 + 2i(\Delta_p - \Delta_c)\right]\Omega_p}{2\left(\Omega_c^2 + \left[\gamma_3 + 2i(\Delta_p - \Delta_c)\right]\left[\gamma_2 + 2i\Delta_p\right]\right)}.$$
(3.29)

The result $\tilde{\rho}_{21}^{\text{st}}$ in the rotating frame has to be transformed back to $\rho_{21}(t)$ in the original frame by using $\rho_{21}(t) = \tilde{\rho}_{21}(\omega_p)e^{-i\omega_p t}$. Then substituting the $\rho_{21}(t)$ into Eq. (3.17), we finally obtain the absorption rate in terms of the imaginary part of susceptibility and we plotted it as a function of the detuning Δ_c in Fig. 2b. We see that the absorption rate of the probe laser decreases once the Rabi oscillation between the level $|2\rangle$ and $|3\rangle$ is induced ($\Delta_c \rightarrow 0$) by the control laser. This means that the Rabi oscillation with frequency $\Omega_c \equiv |\boldsymbol{d}_{23}\cdot\boldsymbol{E}_c|$ between $|2\rangle$ and $|3\rangle$ driven by the control laser $\boldsymbol{E}_c\cos(\omega_c t)$ can interfere with the Rabi oscillation between $|1\rangle$ and $|2\rangle$ and then the Rydberg atoms become effectively transparent (no absorption) for the probe laser. This situation where the probe laser can pass through the Rydberg atoms

Fig. 3 Energy levels of the superheterodyne system. The probe laser induces a Rabi oscillation with a frequency Ω_p between $|1\rangle$ and $|2\rangle$, the control laser induces Rabi oscillation with frequency Ω_p between $|2\rangle$ and $|3\rangle$, and the local laser induces Rabi oscillation with frequency Ω_L between $|3\rangle$ and $|4\rangle$. The electric field induced by GWs with frequency ω_g in the presence of the magnetic field affects the Rabi oscillation between $|3\rangle$ and $|4\rangle$

without being absorbed is called electromagnetically induced transparency (EIT).

The point of the EIT is that the electric field, which couples $|2\rangle$ and $|3\rangle$, significantly alters the absorption rate of the probe laser. Thus, by measuring the changes in the absorption rate of the probe laser, the presence of the electric field that couples $|2\rangle$ and $|3\rangle$ can be detected. This method is further developed into superheterodyne detection method by using a four-level system, which will be explained in the next section.

4 Gravitational wave detector using Rydberg atoms

4.1 Superheterodyne detection strategy

Recently, the authors in [33] proposed a new method to improve the sensitivity further by combining an electromagnetically induced transparency (EIT) method with superheterodyne detection. This superheterodyne detection utilizes four-level Rydberg atoms, each of which consists of two low energy states $|1\rangle$, $|2\rangle$ and two Rydberg states $|3\rangle$, $|4\rangle$ as depicted in Fig. 3. In the superheterodyne method, another transition between $|3\rangle$ and $|4\rangle$ is driven by the strong local laser $\boldsymbol{E}_L \cos(\omega_L t)$. In this case, the Rabi frequency is given by $\Omega_L \equiv |\boldsymbol{d}_{34} \cdot \boldsymbol{E}_L|$. The point here is that this local strong laser induces splitting of the EIT peak called Autler–Townes splitting [36,37], that is, splitting of the peak of absorption rate for the probe laser as we will see in Fig. 5.

Now, let us suppose that GWs arrive to the Rydberg atoms. If we set up a constant magnetic field away from the four-level Rydberg atoms, then a weak electric field signal with frequency ω_g is generated from the interaction between the GWs and the magnetic field. This electric field induces the Rabi oscillation with the frequency $\Omega_g \equiv |\boldsymbol{d}_{34} \cdot \boldsymbol{E}_g|$ between states $|3\rangle$ and $|4\rangle$. As a result, the split absorption rate changes. And this change becomes larger by controlling the local laser as

we will see in Eq. (5.14). By splitting the peak of absorption rate of the probe laser in the superheterodyne method, the sensitivity of the signal of the GW turns out to be improved. By using Eq. (2.7), the Rabi frequency induced by the GWs is given by

$$\Omega_g = |\boldsymbol{d}_{34} \cdot \boldsymbol{E}| = |d_{34}{}^i \varepsilon^{ijk} h^0{}_j B^k| \tag{4.1}$$

Note that $\Omega_g \ll \Omega_L$. This induces a change in the absorption rate of the probe laser when the GWs arrive. More precisely, the frequency shift between the two split peaks can be measured upon the arrival of GWs. In this way, a signal of the GWs can be measured through the change of the absorption rate of the probe laser. We also note that this superheterodyne method is proposed by the authors in [27] for the detection of axion fields.

4.2 Fermi-normal coordinates

In Sect. 2, we considered a constant magnetic field in the laboratory frame. In order to measure GWs that appeared in Eq. (4.1) while maintaining the constant magnetic field, it is necessary to introduce a local inertial system for the GWs. We use Fermi-normal (FN) coordinates that describe the effect of gravity from the point of view of an observer in the laboratory. In the FN coordinate, the metric is perturbatively expanded under the condition that the wavelength of the GWs, λ_g, is much longer than the size of detector L, that is, $\lambda_g \gg L$. However, since the detector becomes the most sensitive for $\lambda_g \sim L$, we need to improve the FN coordinates so that they can incorporate shorter wavelengths of the GWs. The authors in [38–40] made this possible in the case that the GW is a plane wave. Recently, the authors in [41] made use of the improved FN coordinate to detect high-frequency GWs with microwave cavities. It is also shown that the sensitivity of magnon GW detectors can be improved by using the FN coordinates [42]. If we assume that the GW is described by the plane wave $h \propto e^{-i(\omega_g t - \boldsymbol{k} \cdot \boldsymbol{x})}$, the metric components in the FN coordinates are found to be

$$g_{00} = -1 - R_{0i0j}(0)x^i x^j \times 2\Re\left[-\frac{i}{\boldsymbol{k} \cdot \boldsymbol{x}} + \frac{1 - e^{-i\boldsymbol{k} \cdot \boldsymbol{x}}}{(\boldsymbol{k} \cdot \boldsymbol{x})^2}\right], \tag{4.2}$$

$$g_{0i} = -\frac{2}{3} R_{0jik}(0)x^j x^k \times 3\Re\left[-\frac{i}{2(\boldsymbol{k} \cdot \boldsymbol{x})} - \frac{e^{-i\boldsymbol{k} \cdot \boldsymbol{x}}}{(\boldsymbol{k} \cdot \boldsymbol{x})^2} - i\frac{1 - e^{-i\boldsymbol{k} \cdot \boldsymbol{x}}}{(\boldsymbol{k} \cdot \boldsymbol{x})^3}\right], \tag{4.3}$$

$$g_{ij} = \delta_{ij} - \frac{1}{3} R_{ikjl}(0)x^k x^l \times 6\Re\left[-\frac{1 + e^{-i\boldsymbol{k} \cdot \boldsymbol{x}}}{(-\boldsymbol{k} \cdot \boldsymbol{x})^2} - 2i\frac{1 - e^{-i\boldsymbol{k} \cdot \boldsymbol{x}}}{(\boldsymbol{k} \cdot \boldsymbol{x})^3}\right], \tag{4.4}$$

where x^i are spatial coordinates, $k^i x_i = \boldsymbol{k} \cdot \boldsymbol{x}$ and $R_{\mu\nu\rho\sigma}(0)$ is the Riemann tensor evaluated at the origin $x^i = 0$. In order to evaluate Eq. (2.7), we focus on Eq. (4.3). Since the Riemann tensor in Eq. (4.3) is gauge invariant at the linear order, we can express it by the metric in the transverse-traceless (TT) gauge. Then, Eq. (4.3) in the TT gauge, h_{0i}, is calculated as

$$
\begin{aligned}
h_{0i} = \omega_g &\left(k_k h_{ji}^{\mathrm{TT}} \Big|_{\boldsymbol{x}=0} x^j x^k - k_i h_{jk}^{\mathrm{TT}} \Big|_{\boldsymbol{x}=0} x^j x^k \right) \\
&\times \left[\frac{\cos(\boldsymbol{k} \cdot \boldsymbol{x})}{(\boldsymbol{k} \cdot \boldsymbol{x})^2} - \frac{\sin(\boldsymbol{k} \cdot \boldsymbol{x})}{(\boldsymbol{k} \cdot \boldsymbol{x})^3} \right].
\end{aligned} \tag{4.5}
$$

Let us assume that the uniform magnetic field $\boldsymbol{B}$ is pointing only in the positive z direction. Without loss of generality, we can consider the GWs propagating in the z-x plane and its wave vector is given by $\boldsymbol{k} = k(\sin\theta, 0, \cos\theta)$. Then, the polarization tensors $e_{ij}^{(+)}$, $e_{ij}^{(\times)}$ are expressed as

$$
\begin{aligned}
e_{ij}^{(+)} &= \frac{1}{\sqrt{2}} \begin{pmatrix} \cos^2\theta & 0 & -\cos\theta\sin\theta \\ 0 & -1 & 0 \\ -\cos\theta\sin\theta & 0 & \sin^2\theta \end{pmatrix}, \\
e_{ij}^{(\times)} &= \frac{1}{\sqrt{2}} \begin{pmatrix} 0 & \cos\theta & 0 \\ \cos\theta & 0 & -\sin\theta \\ 0 & -\sin\theta & 0 \end{pmatrix}.
\end{aligned} \tag{4.6}
$$

The GWs are then expanded in the form of circularly polarized monochromatic plane-wave,

$$
\begin{aligned}
h_{ij}^{\mathrm{TT}}(t, \boldsymbol{x}) = &h^{(+)} e_{ij}^{(+)} \cos(\omega t - \boldsymbol{k} \cdot \boldsymbol{x}) \\
&+ h^{(\times)} e_{ij}^{(\times)} \cos(\omega t - \boldsymbol{k} \cdot \boldsymbol{x}),
\end{aligned} \tag{4.7}
$$

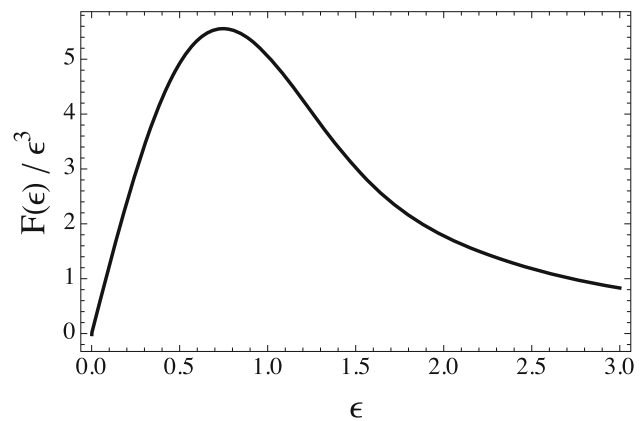where $h^{(+)}$ and $h^{(\times)}$ are the amplitude of the GWs. Substituting Eq. (4.7) into Eq. (4.5), we find

$$
h_{0x} = \omega_g k \frac{h^{(+)}}{\sqrt{2}} \sin\theta \left(y^2 - z^2 \right) \left[\frac{\cos(\boldsymbol{k} \cdot \boldsymbol{x})}{(\boldsymbol{k} \cdot \boldsymbol{x})^2} - \frac{\sin(\boldsymbol{k} \cdot \boldsymbol{x})}{(\boldsymbol{k} \cdot \boldsymbol{x})^3} \right] \tag{4.8}
$$

$$
h_{0y} = \omega_g k \frac{h^{(\times)}}{\sqrt{2}} \cos\theta\sin\theta \left(x^2 - z^2 \right) \left[\frac{\cos(\boldsymbol{k} \cdot \boldsymbol{x})}{(\boldsymbol{k} \cdot \boldsymbol{x})^2} - \frac{\sin(\boldsymbol{k} \cdot \boldsymbol{x})}{(\boldsymbol{k} \cdot \boldsymbol{x})^3} \right] \tag{4.9}
$$

where we ignored the terms involving $x^j x^k = xy, yz, zx$ in Eq. (4.5) because they vanish when averaging h_{0i} over the size of detector. Suppose that the size of the detector consisting of the Rydberg atoms is L. We average Eqs. (4.8) and (4.9) over the size of detector radius $\ell = L/2$ in spherical coordinates (r, ζ, ϕ). The details of the calculations are presented in the Appendix A where we introduced a dimensionless parameter $\epsilon = \ell/\lambda_g = k\ell/(2\pi)$ and a variable $r' = r/\ell$. The spherically-averaged h_{0i} over the size of detector is given in the form

$$
\langle h_{0x} \rangle = \frac{h^{(+)}}{\sqrt{2}} \sin\theta\, F(\epsilon) \tag{4.10}
$$

$$
\langle h_{0y} \rangle = \frac{h^{(\times)}}{\sqrt{2}} \cos\theta\sin\theta\, F(\epsilon) \tag{4.11}
$$

Fig. 4 Plot of $F(\epsilon)/\epsilon^3$ as a function of $\epsilon = \ell/\lambda_g = k\ell/(2\pi) = \omega_g\ell/(2\pi)$, which takes the maximum at $\epsilon \sim 0.7$. Therefore, when the ratio of cell size to gravitational wave wavelength is around 0.7, the Rabi frequency is maximized, leading to the highest sensitivity. Adjusting the size of the cell to match the target gravitational wave wavelength optimizes sensitivity

where we used $\omega_g = k$ and defined $F(\epsilon)$ as

$$
\begin{aligned}
F(\epsilon) \equiv &\frac{\pi \left(\pi^2\epsilon^2 - 3 \right) \mathrm{Si}(2\pi\epsilon)}{2\pi\epsilon} + \frac{\pi \left(2\pi^2\epsilon^2 - 15 \right) \cos(2\pi\epsilon)}{8\pi^2\epsilon^2} \\
&+ \frac{\pi \left(2\pi^2\epsilon^2 + 15 \right) \sin(2\pi\epsilon)}{16\pi^3\epsilon^3}.
\end{aligned} \tag{4.12}
$$

Here, $\mathrm{Si}(\epsilon)$ is the sine integral defined as $\mathrm{Si}(x) = \int_0^x dt \sin t/t$. We plotted $F(\epsilon)/\epsilon^3$ as a function of ϵ in Fig. 4. Finally, the averaged Rabi frequency Ω_g is calculated such as

$$
\begin{aligned}
\langle \Omega_g \rangle &= \left\langle |\boldsymbol{d}^{(34)} \cdot \boldsymbol{E}| \right\rangle = |d^{(34)i} \varepsilon^{ijk} \langle h^0{}_j \rangle B^k| \\
&= F(\epsilon) \frac{B_z}{\sqrt{2}} \left| \sin\theta \left[d_x^{(34)} h^{(\times)} \cos\theta - d_y^{(34)} h^{(+)} \right] \right|. \tag{4.13}
\end{aligned}
$$

For long-wavelength GWs ($\epsilon \ll 1$), the sensitivity of the detector to the GWs is significantly reduced due to the rapid decay of $F(\epsilon)$ as shown in Fig. 4. This reflects the equivalence principle for the detector. On the other hand, for short-wavelength GWs ($\epsilon \gg 1$), $F(\epsilon)$ increases as $F(\epsilon) \propto \epsilon$. However, as the wavelength of the GWs becomes shorter, the number of Rydberg atoms within the wavelength decreases at a rate proportional to its volume ϵ^{-3}. Hence, the sensitivity is reduced by ϵ^{-3}. As a result, the sensitivity of the detector is maximized at $\epsilon \sim 0.7$.

5 The minimum detectable amplitude of GWs

In this section, we evaluate the sensitivity of the GW detector with heterodyne receivers. A signal of the GWs is measured by a change in the absorption rate of the probe laser. As mentioned in Sect. 3.2, the absorption rate is proportional to the imaginary part of electric susceptibility which can be related to the density operator of an atom. Thus, we calculate

the density operator for the Rydberg four-level system, and then, we evaluate the minimum detectable amplitude of GWs.

5.1 Master equation for Rydberg system

As we explained in the Sect. 4.1, we consider a four-level Rydberg atom that consists of two low energy states $|1\rangle$, $|2\rangle$ and two Rydberg states $|3\rangle$, $|4\rangle$ as depicted in Fig. 3. The total Hamiltonian $\hat{H}(t)$ for the four-level atom interacting with probe laser, control laser, strong local laser and GWs is written as

$$\hat{H}(t) = \hat{H}_0 + \hat{H}'(t) \tag{5.1}$$

with the unperturbed Hamiltonian

$$\hat{H}_0 = \varepsilon_1 |1\rangle \langle 1| + \varepsilon_2 |2\rangle \langle 2| + \varepsilon_3 |3\rangle \langle 3| + \varepsilon_4 |4\rangle \langle 4|, \tag{5.2}$$

where ε_i with $i = 1, 2, 3, 4$ denotes the energy of each level. The dipole interaction Hamiltonian reads

$$\hat{H}'(t) = -\frac{\Omega_p}{2} e^{-i\omega_p t} |2\rangle \langle 1| - \frac{\Omega_c}{2} e^{-i\omega_c t} |3\rangle \langle 2|$$
$$- \left(\frac{\Omega_L}{2} e^{-i\omega_L t} + \frac{\Omega_g}{2} e^{-i\omega_g t} \right) |3\rangle \langle 4| + \text{h.c.} \tag{5.3}$$

where Ω_p, Ω_c, Ω_L, and Ω_g, are Rabi frequencies associated with the transitions $|1\rangle \rightarrow |2\rangle$, $|2\rangle \rightarrow |3\rangle$ and $|3\rangle \rightarrow |4\rangle$, respectively. Using the unitary operator

$$\hat{U} \equiv \exp\Big[i\varepsilon_1 |1\rangle \langle 1| t + i (\varepsilon_1 + \omega_p) |2\rangle \langle 2| t$$
$$+ i(\varepsilon_1 + \omega_p + \omega_c) |3\rangle \langle 3| t + i(\varepsilon_1 + \omega_p + \omega_c - \omega_L) |4\rangle \langle 4| t \Big] \tag{5.4}$$

we obtain the Hamiltonian in the rotating frame
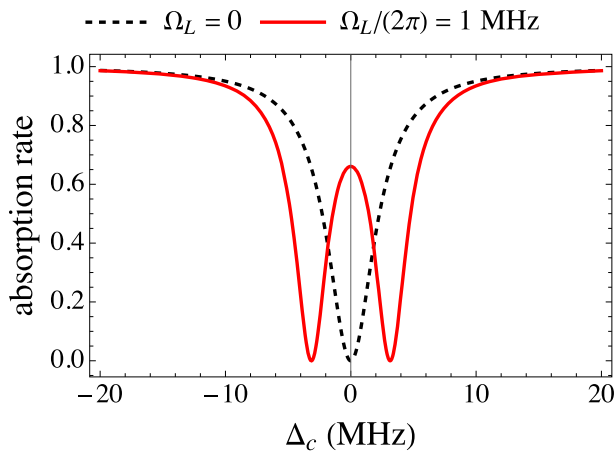
$$\hat{\mathcal{H}} = \Delta_p |2\rangle \langle 2| + (\Delta_p + \Delta_c) |3\rangle \langle 3| + (\Delta_p + \Delta_c + \Delta_L) |4\rangle \langle 4|$$
$$+ \left[-\frac{\Omega_p}{2} |2\rangle \langle 1| - \frac{\Omega_c}{2} |3\rangle \langle 2| - \frac{\Omega_L + \Omega_g e^{-i\delta_g t}}{2} |3\rangle \langle 4| + \text{h.c.} \right] \tag{5.5}$$

where we defined detunings Δ_p, Δ_c, Δ_L, and δ_g by

$$\Delta_p \equiv (\varepsilon_2 - \varepsilon_1) - \omega_p \tag{5.6}$$
$$\Delta_c \equiv (\varepsilon_3 - \varepsilon_2) - \omega_c \tag{5.7}$$
$$\Delta_L \equiv \omega_L - (\varepsilon_3 - \varepsilon_4) \tag{5.8}$$
$$\delta_g \equiv \omega_g - \omega_L. \tag{5.9}$$

Note that the time dependence except for δ_g in the Hamiltonian was eliminated in this rotating frame. The master equation for total system in the rotating frame $\tilde{\rho}$ is given by

$$\frac{d}{dt} \tilde{\rho} = -i[\hat{\mathcal{H}}, \tilde{\rho}] + \sum_{k=2,3,4} \gamma_k \left[\hat{O}_k \tilde{\rho} \hat{O}_k^\dagger - \frac{1}{2} \left\{ \hat{O}_k^\dagger \hat{O}_k, \tilde{\rho} \right\} \right]$$
$$+ (\gamma_2 \tilde{\rho}_{22} + \gamma_4 \tilde{\rho}_{44}) |1\rangle \langle 1| + \gamma_3 \tilde{\rho}_{33} |2\rangle \langle 2| \tag{5.10}$$

where $\hat{O}_k = |1\rangle \langle k|$ represents the relaxation process of the atom, and the third and the fourth term in the right hand side represent repopulation processes.

Let us consider the resonance case $\Delta_L = 0$. We can assume that $\gamma_3 = \gamma_4 = 0$ because the relations $\gamma_3, \gamma_4 \ll \gamma_2$ hold in general. Then, the stationary state solution of the master equation $\tilde{\rho}_{21}^{\text{st}}$ is

$$\frac{\tilde{\rho}_{21}^{\text{st}}}{\tilde{\rho}_{11}} = \frac{\left[4 (\Delta_p + \Delta_c)^2 - \Omega^2 \right] \left[-8\Delta_p (\Delta_p + \Delta_c)^2 + 2 (\Delta_p + \Delta_c) \Omega_c^2 + 2\Delta_p \Omega^2 \right] \Omega_p}{A'\Delta_c^4 + B'\Delta_c^3 + C'\Delta_c^2 + D'\Delta_c + E'}$$
$$+ i \frac{\gamma_2 \left[4 (\Delta_p + \Delta_c)^2 - \Omega^2 \right]^2 \Omega_p}{A'\Delta_c^4 + B'\Delta_c^3 + C'\Delta_c^2 + D'\Delta_c + E'} \tag{5.11}$$

where we defined A', B', C', D', and E' as

$$A' = 16 \left(4\Delta_p^2 + \Omega_p^2 + \gamma_2^2 \right)$$
$$B' = 256\Delta_p^3 + 32\Delta_p \left(2\Omega_p^2 - \Omega_c^2 + 2\gamma_2^2 \right)$$
$$C' = 384\Delta_p^4 + 32\Delta_p^2 \left(3\Omega_p^2 - 3\Omega_c^2 - \Omega^2 + 3\gamma_2^2 \right)$$
$$+ 4 \left(\Omega_p^2 \Omega_c^2 - 2\Omega_p^2 \Omega^2 + \Omega_c^4 - 2\Omega^2 \gamma_2^2 \right)$$
$$D' = 256\Delta_p^5 + 32\Delta_p^3 \left(2\Omega_p^2 - 3\Omega_c^2 - 2\Omega^2 + 2\gamma_2^2 \right)$$
$$+ 8\Delta_p \left(\Omega_p^2 \Omega_c^2 - 2\Omega_p^2 \Omega^2 + \Omega_c^4 + \Omega_c^2 \Omega^2 - 2\Omega^2 \gamma_2^2 \right)$$
$$E' = 64\Delta_p^6 + 16\Delta_p^4 \left(\Omega_p^2 - 2\Omega_c^2 - 2\Omega^2 + \gamma_2^2 \right)$$
$$+ 4\Delta_p^2 \left(\Omega_p^2 \Omega_c^2 - 2\Omega_p^2 \Omega^2 + \Omega_c^4 + 2\Omega_c^2 \Omega^2 \right.$$
$$\left. + \Omega^4 - 2\Omega^2 \gamma_2^2 \right) + \Omega_p^2 \Omega_c^2 \Omega^2 + \Omega_p^2 \Omega^4 + \Omega^4 \gamma_2^2. \tag{5.12}$$

Here we introduced $\Omega \equiv \Omega_L + \Omega_g e^{-i\delta_g t}$ which is almost constant because of the relation $\Omega_g \ll \Omega_L$.

Fig. 5 Plots of the absorption rate of the probe laser as a function of Δ_c. Here we used $\gamma_2/(2\pi) = 5.2$ MHz, $\gamma_3/(2\pi) = 3.9$ kHz, $\gamma_4/(2\pi) = 1.7$ kHz, $\Omega_p/(2\pi) = 5.7$ MHz, $\Omega_c/(2\pi) = 0.97$ MHz, $\Omega_L/(2\pi) = 1.0$ MHz [33]. The absorption rate is defined as $\Im\chi/(\Im\chi)_{max}$. The splitting of the peak of absorption rate for the probe laser occurs due to the local laser

The result $\tilde{\rho}_{21}^{st}$ in the rotating frame has to be transformed back to $\rho_{21}(t)$ in the original frame by using $\rho_{21}(t) = \tilde{\rho}_{21}(\omega_p)e^{-i\omega_p t}$. Substituting $\rho_{21}(t)$ into Eq. (3.17), we finally obtain the absorption rate in terms of the imaginary part of susceptibility in the form.

$$\Im\chi = \frac{2N|\boldsymbol{d}_{12}|^2}{\Omega_p} \frac{\gamma_2\left[4\left(\Delta_p + \Delta_c\right)^2 - \Omega^2\right]}{A\Delta_c^4 + B\Delta_c^3 + C\Delta_c^2 + D\Delta_c + E}. \quad (5.13)$$

The absorption rate, defined as $\Im\chi/(\Im\chi)_{max}$, is shown in Fig. 5. It can be seen that the local laser causes the AT splitting. This is a phenomenon that does not occur in the three-level EIT system, and is a feature of the superheterodyne system.

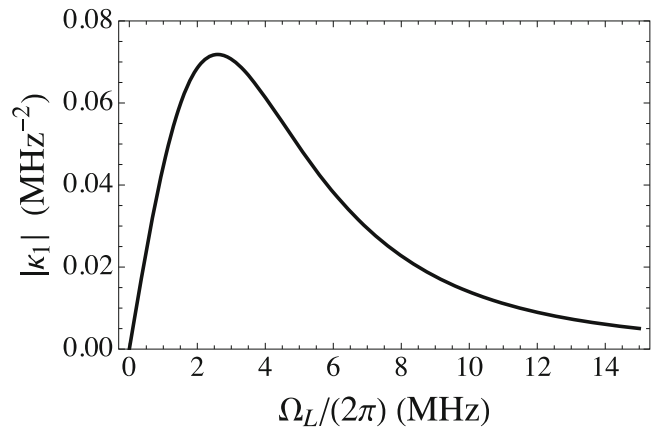### 5.2 Estimation of the minimum detectable GW amplitude

To evaluate the minimum detectable amplitude of GWs, we restore the time-dependence of Ω in Eq. (5.13). We can expand $|\Omega|^2$ up to the first order in Ω_g such as

$$|\Omega^2| = \left(\Omega_L + \Omega_g e^{-i\delta_g t}\right)\left(\Omega_L + \Omega_g e^{i\delta_g t}\right) \sim \Omega_L^2 + 2\Omega_L\Omega_g\cos\delta_g t.$$

Plugging the result into Eq. (5.13), we find

$$\Im\chi = 2N|\boldsymbol{d}_{12}|^2\kappa_0 + 2N|\boldsymbol{d}_{12}|^2\kappa_1\Omega_g\cos(\delta_g t) \quad (5.14)$$

where κ_0 and κ_1 depend on the Rabi frequencies Ω_p, Ω_c, Ω_L, the detunings Δ_p, Δ_c and relaxation rate γ_2 and can be calculated as

Fig. 6 Plot of $|\kappa_1|$ as a function of the Rabi frequency Ω_L normalized by 2π in which the resonance condition $\Delta_p = \Delta_c = \Delta_L = 0$ is imposed. Other parameters are set to $\gamma_2/(2\pi) = 5.2$ MHz, $\gamma_3 = \gamma_4 = 0$, $\Omega_p/(2\pi) = 5.7$ MHz, $\Omega_c/(2\pi) = 0.97$ MHz, $\Omega_L/(2\pi) = 1.0$ MHz. This plot shows that $|\kappa_1|$ becomes the maximum value 0.072 MHz^{-2} at the Rabi frequency $\Omega_L/(2\pi) = 2.6$ MHz. The minimum detectable amplitude of the GWs, associated with these values, can be measured

$$\kappa_0 = \frac{1}{\Omega_p}\Im\rho_{12}\left(\Omega_L^2\right), \qquad \kappa_1 = 2\frac{\Omega_L}{\Omega_p}\frac{d\Im\rho_{21}(x)}{dx}\bigg|_{x=\Omega_L^2}. \quad (5.15)$$

Note that κ_1 represents a change of absorption rate of the probe laser due to the GWs. Notice that κ_1 would not exist without the local laser. We plotted the Ω_L dependence of κ_1 in Fig. 6. We see $|\kappa_1|$ takes the maximum value 0.072 MHz^{-2} for $\Omega_L/(2\pi) = 2.6$ MHz.

By using Eqs. (3.9) and (3.11), the output power of the probe laser $P(t)$ is calculated as $P(t) = |E(z,t)|^2 = |E_0|^2 e^{-2\omega_p\kappa z} = P_i e^{-\omega_p L\Im\chi}$, where $P_i (= |E_0|^2)$ is input power of the probe laser, L is the size of Rydberg atoms and we set $n = 1$, $z = L$. Substituting Eq. (5.14) into $P(t)$, we find

$$\begin{aligned}
P(t) &= P_i e^{-\omega_p L 2N|\boldsymbol{d}_{12}|^2\kappa_0} e^{-\omega_p L 2N|\boldsymbol{d}_{12}|^2\kappa_1\Omega_g\cos(\omega_g t)} \\
&\approx P_i e^{-\omega_p L 2N|\boldsymbol{d}_{12}|^2\kappa_0} \\
&\quad - P_i e^{-\omega_p L 2N|\boldsymbol{d}_{12}|^2\kappa_0} \cdot 2N|\boldsymbol{d}_{12}|^2\omega_p L\kappa_1\Omega_g\cos(\omega_g t) \\
&\equiv P_0 + 2P_0 N|\boldsymbol{d}_{12}|^2\omega_p L\kappa_1\Omega_g\cos(\delta_g t), \quad (5.16)
\end{aligned}$$

where $P_0 \equiv P_i e^{-\omega_p L 2N|\boldsymbol{d}_{12}|^2\kappa_0}$. Now, we estimate the minimum detectable electric field. Note that a signal can be measured when the ratio of the stationary term to the oscillation term of the Eq. (3.31) is greater than 1. Thus, the minimum detectable Rabi-frequency $\Omega_{g\,(min)}$ satisfies the following equation.

$$\frac{2P_0 N|\boldsymbol{d}_{12}|^2\omega_p L|\kappa_1|\Omega_g\cos(\delta_g)}{P_0} = 1. \quad (5.17)$$

Combining it with the relation $\Omega_{g \, (\min)} = |\boldsymbol{d}_{34} \cdot \boldsymbol{E}_{\min}|$, we find the minimum magnitude of the detectable electric field as

$$E_{\min} = \frac{\Omega_{g \, (\min)}}{|\boldsymbol{d}_{34}|} = \frac{1}{2|\boldsymbol{d}_{34}||\boldsymbol{d}_{12}|^2 N \omega_p L |\kappa_1|}. \tag{5.18}$$

Let us estimate the minimum detectable value. We consider Rubidium atoms with the four levels $|1\rangle \, : \, 5S_{1/2}$, $|2\rangle \, : \, 5P_{3/2}$, $|3\rangle \, : \, 59P_{3/2}$, and $|4\rangle \, : \, 57D_{5/2}$. In this case, the dipole moment and the energy gap are calculated as $|\boldsymbol{d}_{12}| = 5.158 e a_0$, $\varepsilon_2 - \varepsilon_1 = 384$ THz, $|\boldsymbol{d}_{34}| = 2416 e a_0$, and $\varepsilon_3 - \varepsilon_4 = 26.4$ GHz. Here, e is a electric charge and a_0 is the Bohr radius, and we used Alkari Rydberg Calculator (ARC) package [43] to calculate the dipole moment. According to [44], N can be increased up to $N \sim 1.6 \times 10^{14}$ cm^{-3}. The size of the Rydberg atoms is $L = 2\ell = 10$ cm. Thus, we obtain

$$\begin{aligned}
\frac{E_{\min}}{\sqrt{\text{Hz}}} &= 8.8 \times 10^{-17} \text{ eV}^2/\sqrt{\text{Hz}} \left(\frac{2416 \, e a_0}{|\boldsymbol{d}_{34}|} \right) \\
&\times \left(\frac{5.158 \, e a_0}{|\boldsymbol{d}_{12}|} \right)^2 \left(\frac{1.6 \times 10^{14} \text{ cm}^{-3}}{N} \right) \\
&\times \left(\frac{384 \text{ THz}}{\omega_p} \right) \left(\frac{10 \text{ cm}}{L} \right) \left(\frac{0.072 \text{ MHz}^{-2}}{|\kappa_1|} \right).
\end{aligned} \tag{5.19}$$

Thus, the minimum detectable electric fields turn out to be $E_{\min} = 8.8 \times 10^{-17} \text{ eV}^2/\sqrt{\text{Hz}} = 1.4 \text{ pV}/(\text{cm} \cdot \sqrt{\text{Hz}})$.

Next we estimate the minimum detectable amplitude of GWs. In Eq. (4.13), to consider the most favourable situation, we choose $\theta = \pi/2$ that represents the situation where GWs propagate in the direction perpendicular to the magnetic field. In this case, from Eq. (4.13), h is expressed as

$$\begin{aligned}
\frac{h_{\min}}{\sqrt{\text{Hz}}} &= \frac{1}{\sqrt{\text{Hz}}} \frac{\sqrt{2} \langle \Omega_g \rangle}{|\boldsymbol{d}_{34}| B_z F(\epsilon)} \\
&= \frac{1}{\sqrt{\text{Hz}}} \frac{\sqrt{2}}{2} \frac{1}{B_z F(\epsilon) |\boldsymbol{d}_{34}||\boldsymbol{d}_{12}|^2 N \omega_p L |\kappa_1|}.
\end{aligned} \tag{5.20}$$

Here, we take $B_z = 10$ T. The energy gap of the two Rydberg states determines the detectable frequency of the GWs, $\omega_g \sim \varepsilon_4 - \varepsilon_3 = 26.4$ GHz, which corresponds to the wavelength $\lambda_g = 1.14$ cm. When the size of the Rydberg atoms is $L = 2\ell = 10$ cm, then the value of $F(\epsilon)$ at $\epsilon = \omega_g \ell/2\pi = 0.701$ becomes $F(0.701) \simeq 1.91$. Thus, the minimum detectable amplitude of the GWs by using the Rydberg atoms turns out to be

$$\begin{aligned}
\frac{h_{\min}}{\sqrt{\text{Hz}}} &= 2.8 \times 10^{-20} \frac{1}{\sqrt{\text{Hz}}} \left(\frac{1.91}{F(\epsilon)} \right) \left(\frac{10 \text{ T}}{B_z} \right) \\
&\times \left(\frac{2416 \, e a_0}{|\boldsymbol{d}_{34}|} \right) \left(\frac{5.158 \, e a_0}{|\boldsymbol{d}_{12}|} \right)^2 \\
&\times \left(\frac{1.6 \times 10^{14} \text{ cm}^{-3}}{N} \right) \left(\frac{384 \text{ THz}}{\omega_p} \right) \left(\frac{10 \text{ cm}}{L} \right) \\
&\times \left(\frac{0.072 \text{ MHz}^{-2}}{|\kappa_1|} \right).
\end{aligned} \tag{5.21}$$

Finally, let us estimate the minimum detectable amplitude of GWs in the quantum projection noise limit based on [45]. The basic idea of the EIT is to measure the frequency shift between the two split peaks $\Delta \nu$ which is related to the amplitude of electric field E and electric dipole moment d as

$$E \simeq \frac{\Delta \nu}{d}. \tag{5.22}$$

Since $\Delta \nu \sim 1/(\sqrt{n} \, T_2)$, where T_2 is the coherence time of the EIT and n is the number of independent measurement taking place per second, we obtain

$$E \simeq \frac{1}{d \sqrt{n} T_2}. \tag{5.23}$$

Let T be the integration time of the coherent EIT process. Then, we can deduce

$$n = N_a \frac{T}{T_2} \tag{5.24}$$

where N_a is the number of atoms participating in the measurement per second. Hence, the minimum detectable electric field in the quantum projection noise limit (QPNL) is given by

$$E_{\min} = \frac{1}{d \sqrt{N_a T T_2}}. \tag{5.25}$$

Setting $T = 1$s gives the sensitivity limit

$$E_{\text{QPNL}} = \frac{E_{\min}}{\sqrt{\text{Hz}}} = \frac{1}{d \sqrt{N_a T_2}}. \tag{5.26}$$

The dipole moment is $d = |\boldsymbol{d}_{34}| = 2416 e a_0 \sim 3.87 \times 10^{-6}$ cm. The number of atoms participating in the measurement is $N_a = 2.14 \times 10^{13}$ s^{-1} [33], and the coherence time of Rydberg atom EIT system is $T_2 = 100$ ns [44]. Thus, we obtain

$$\begin{aligned}
E_{\text{QPNL}} &= 1.7 \times 10^{-1} \text{ pV}/(\text{cm} \cdot \sqrt{Hz}) \\
&\times \left(\frac{3.87 \times 10^{-6} \text{ cm}}{d} \right) \left(\frac{2.14 \times 10^{13} \text{ s}^{-1}}{N_a} \right)^{1/2} \\
&\times \left(\frac{100 \text{ ns}}{T_2} \right)^{1/2}.
\end{aligned} \tag{5.27}$$

This can be translated to the amplitude of GWs as

$$h_{\text{QPNL}} = 3.4 \times 10^{-21} \frac{1}{\sqrt{\text{Hz}}} \left(\frac{1.91}{F(\epsilon)} \right) \left(\frac{10\,\text{T}}{B_z} \right)$$
$$\times \left(\frac{3.87 \times 10^{-6}\,\text{cm}}{d} \right) \left(\frac{2.14 \times 10^{13}\,\text{s}^{-1}}{N_a} \right)^{1/2}$$
$$\times \left(\frac{100\,\text{ns}}{T_2} \right)^{1/2} . \tag{5.28}$$

For instance, we can expect ultimate value 1.7 fV/cm for $T = 10^4$ s. This number can be translated into the GW amplitude $h \sim 10^{-23}$.

We note that one of the noise sources is thermal black-body radiation. However, background electromagnetic waves can be shielded by enclosing the detector in metal, so they do not become a source of noise that would affect the sensitivity. Although other significant sources of noise include laser amplitude fluctuations and measurement noise, according to [46], shot noises and measurement noises can be neglected. Therefore, the fundamental noise limit is determined by the quantum projection noise limit Eq. (5.28). Note that we are evaluating the minimum detectable GW amplitude in an ideal scenario where mutual interactions between Rydberg atoms are neglected. A future challenge will be to estimate, both experimentally and theoretically, how interactions between atoms affect sensitivity.

5.3 Comparison with other detectors

The detector with Rydberg atoms has some advantages. For instance, it is possible to adjust the detectable frequencies of GWs by tuning the energy level of $|3\rangle$ and $|4\rangle$ and the size of the cell of Rydberg atoms. We would be able to prepare multiple cells of Rydberg detectors and set each one to target gravitational waves at different frequencies. Thus, GW detector by Rydberg atoms make us possible to detect a wide range of frequencies. It is possible to search for GWs in the angular frequency range between 2 and 100 GHz, which corresponds to the frequency range between 0.3 GHz and 16 GHz. The lower limit is determined by the minimum energy level gap between $|3\rangle$ and $|4\rangle$, which arises from the fact that the principal quantum number of maximum excitation in a Rydberg atom is $\mathcal{O}(90)$. The upper limit, on the other hand, is determined by the sensitivity. At frequencies higher than around 16 GHz, the minimum amplitude of the detectable GWs becomes above 10^{-19}. Hence it would be difficult to detect GWs. Their minimum detectable amplitude can be estimated from Eq. (5.28). The sensitivity and the range of observable frequencies of various detectors are shown in Fig. 7 where we can see the Rydberg detector can cover a wide range of GWs.

Let us compare the sensitivity of the detector proposed in this study with that of a similar detection method for

axion dark matter using Rydberg atoms [27]. In [27], they claim that the minimum detectable electric field is $|\boldsymbol{E}| = 300$ pV/cm, $|\boldsymbol{E}| = 5.0$ pV/cm and $|\boldsymbol{E}| = 0.18$ pV/cm for measurement times of 1 s, 1 h and 1 month, respectively. Since the minimum measurable amplitude of our detector is $E_{\min} \sim 1.4$ pV/cm as shown in (5.19), our result is consistent with that in [27]. Furthermore, the microwave cavities proposed in [41], specifically ADMX, achieve a detection sensitivity of $h \sim 10^{-21}$. When converted to electric field detection sensitivity, we obtain
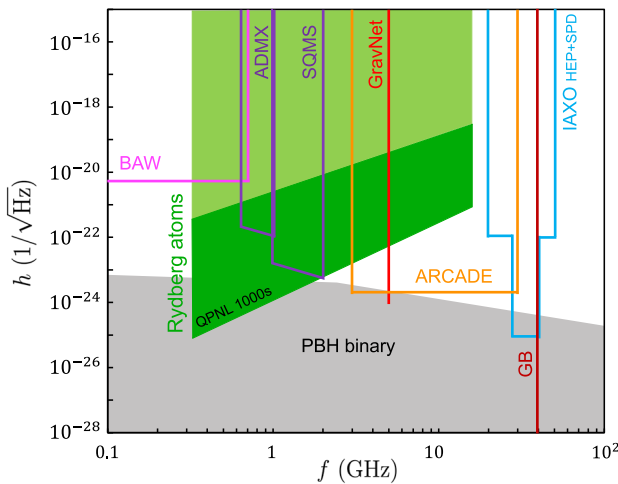
$$E_{\text{min,cav}} \sim 10^{-18}\,\text{eV}^2 \left(\frac{B}{7.5\,\text{T}} \right) \left(\frac{h}{10^{-21}} \right)$$

which corresponds to approximately 0.01 pV/cm. Therefore, cavity-based detectors offer superior sensitivity compared to detectors utilizing Rydberg atoms. Note that although the electric field sensitivity given by (5.19) (represented by the light green region in Fig. 7) does not show a significant advantage, the frequency range of Rydberg detectors is broader than that of cavity detectors.

On the other hand, in an idealized scenario where the detector sensitivity is determined by the quantum projection noise limit as given by Eq. (5.27), the minimum detectable electric field is evaluated as $E_{\min} \sim 1.7$ fV/cm for a measurement time 1000 s. In this case, the sensitivity is represented by the dark green region in Fig. 7. We can see that the detector using Rydberg atoms demonstrates superior sensitivity across a broad frequency range compared to other detectors.

6 Conclusion

We studied high-frequency GW detectors with Rydberg atoms. First, we showed that a weak electric field signal is generated from GWs in the presence of the magnetic field. We calculated the effective electric field induced by GWs using improved Fermi-normal coordinates with which we can treat GWs with wavelength shorter than the detector size. We then explained the electromagnetically induced transparency (EIT) employed for detecting electric fields. The method is further improved by combining the superheterodyne detection method in the system of Rydberg atoms. The weak signal of the GWs can be probed by measuring the absorption rate of the probe laser. We showed that the absorption rate is proportional to the imaginary part of electric susceptibility, and that the susceptibility can be related to the density operator of the Rydberg atom. Considering two low energy states $|1\rangle$, $|2\rangle$ and two Rydberg states $|3\rangle$, $|4\rangle$, we obtain the absorption rate of the probe laser in terms of the imaginary part of the susceptibility. We evaluated the ratio of the output power with a signal of GWs to that with no signal GWs. Finally, we evaluated the the minimum measurable GW amplitude with Rubidium Rydberg atoms and found that GWs with the

Fig. 7 An overview of the characteristic strain for gravitational wave detector in the frequency range between 0.1 and 100 GHz. Light green region is for the superheterodyne method with Rydberg atoms. Dark green region is for the quantum projection noise limit(QPNL) in a 1000s measurement with Rydberg atoms. The sensitivity of bulk acoustic wave devices (BAW) [47,48] are shown in light red line. The sensitivity of microwave cavities from ADMX [49] and SQMS [41] is shown in purple. Global network of cavities(GravNet) [50] is shown in red. The sensitivity of the ARCADE 2 [51] is shown in orange, IAXO HEP and IAXO SPD [52] are shown in light blue, and EM Gaussian beams(GB) [53] is shown in brown. The grey region shows the gravitational waves emitted from the primordial blake hole (PBH) binary [54]

amplitude 10^{-20} and the angular frequency 26.4 GHz can be detected.

The advantage of using the GW detector with Rydberg atoms is its broad detectable frequency band due to the flexibility of adjusting the detector size. Tuning the energy levels of $|3\rangle$ and $|4\rangle$ and the size of the cell of Rydberg atoms, we can detect GWs with a frequency in the range between 0.3 GHz and 16 GHz.

Data Availability Statement This manuscript has no associated data. [Authors' comment: There are no datasets associated with this study.]

Code Availability Statement This manuscript has no associated code/software. [Authors' comment: There are no codes associated with this study.]

Appendix A: Rabi frequency stemming from GWs

When we derive Eqs. (4.10) and (4.11), we perform integration in spherical coordinates (r, ζ, ϕ) as follows.

For $i = x$, we can calculate as

$$
\begin{aligned}
k_k h_{ji}^{\mathrm{TT}} x^j x^k &= k \sin\theta \left(h_{xx} xx + h_{yx} yx + h_{zx} zx \right) \\
&\quad + k \cos\theta \left(h_{xx} xz + h_{yx} yz + h_{zx} zz \right) \\
&= k \sin\theta \left(\frac{h^{(+)}}{\sqrt{2}} \cos^2\theta\, xx + \frac{h^{(\times)}}{\sqrt{2}} \cos\theta\, yx \right. \\
&\quad \left. - \frac{h^{(+)}}{\sqrt{2}} \cos\theta \sin\theta\, zx \right) \\
&\quad + k \cos\theta \left(\frac{h^{(+)}}{\sqrt{2}} \cos^2\theta\, xz + \frac{h^{(\times)}}{\sqrt{2}} \cos\theta\, yz \right. \\
&\quad \left. - \frac{h^{(+)}}{\sqrt{2}} \cos\theta \sin\theta\, zz \right),
\end{aligned}
\tag{A.1}
$$

and

$$
\begin{aligned}
k_i h_{jk}^{\mathrm{TT}} x^j x^k &= k_x h_{xx} xx + k_x h_{yy} yy + k_x h_{zz} zz + 2k_x h_{xy} xy \\
&\quad + 2k_x h_{yz} yz + 2k_x h_{zx} zx \\
&= k \sin\theta \left(\frac{h^{(+)}}{\sqrt{2}} \cos^2\theta\, xx - \frac{h^{(+)}}{\sqrt{2}} yy \right. \\
&\quad + \frac{h^{(+)}}{\sqrt{2}} \sin^2\theta\, zz + 2\frac{h^{(\times)}}{\sqrt{2}} \cos\theta\, xy \\
&\quad \left. - 2\frac{h^{(\times)}}{\sqrt{2}} \sin\theta\, yz - 2\frac{h^{(\times)}}{\sqrt{2}} \cos\theta \sin\theta\, zx \right).
\end{aligned}
\tag{A.2}
$$

When integrating with respect to ϕ in spherical coordinates, terms involving xy, xz, yz will be zero. Thus we obtain

$$
\begin{aligned}
h_{0x} &= \omega_g k \left(-\frac{h^{(+)}}{\sqrt{2}} \cos^2\theta \sin\theta\, z^2 + \frac{h^{(+)}}{\sqrt{2}} \sin\theta\, y^2 - \frac{h^{(+)}}{\sqrt{2}} \sin^3\theta\, z^2 \right) \\
&\quad \times \left[\frac{\cos(\boldsymbol{k}\cdot\boldsymbol{x})}{(\boldsymbol{k}\cdot\boldsymbol{x})^2} - \frac{\sin(\boldsymbol{k}\cdot\boldsymbol{x})}{(\boldsymbol{k}\cdot\boldsymbol{x})^3} \right], \\
&= \omega_g k \frac{h^{(+)}}{\sqrt{2}} \sin\theta \left(y^2 - z^2 \right) \left[\frac{\cos(\boldsymbol{k}\cdot\boldsymbol{x})}{(\boldsymbol{k}\cdot\boldsymbol{x})^2} - \frac{\sin(\boldsymbol{k}\cdot\boldsymbol{x})}{(\boldsymbol{k}\cdot\boldsymbol{x})^3} \right].
\end{aligned}
\tag{A.3}
$$

We align the z-axis with the direction of $\boldsymbol{k}$ and introduce a spherical coordinate system. We then convert the Carte-

sian coordinate to the spherical coordinate by using $x = r \sin\zeta \cos\phi$, $y = r \sin\zeta \sin\phi$, $z = r \cos\zeta$. Using $\omega_g = k$, $\bar{\epsilon} = k\ell$, $r' = r/\ell$, we can take average

$$
\begin{aligned}
\langle h_{0x} \rangle &= \frac{h^{(+)}}{\sqrt{2}} \sin\theta \int_0^1 \int_0^\pi \int_0^{2\pi} dr' d\zeta\, d\phi\, r'^2 \sin\zeta \\
&\quad \times \left(\tan^2\zeta \sin^2\phi - 1 \right) \left[\cos(\bar{\epsilon} r' \cos\zeta) - \frac{\sin(\bar{\epsilon} r' \cos\zeta)}{\bar{\epsilon} r' \cos\zeta} \right] \\
&= \frac{h^{(+)}}{\sqrt{2}} \sin\theta\, F(\bar{\epsilon})
\end{aligned}
$$
(A.4)

where we defined

$$
\begin{aligned}
\bar{F}(\bar{\epsilon}) &\equiv \frac{\pi \left(\bar{\epsilon}^2 - 12 \right) \mathrm{Si}(\bar{\epsilon})}{4\bar{\epsilon}} + \frac{\pi \left(\bar{\epsilon}^2 - 30 \right) \cos(\bar{\epsilon})}{4\bar{\epsilon}^2} \\
&\quad + \frac{\pi \left(\bar{\epsilon}^2 + 30 \right) \sin(\bar{\epsilon})}{4\bar{\epsilon}^3}.
\end{aligned}
$$
(A.5)

For $i = y$, we can deduce

$$
k_i h^{\mathrm{TT}}_{jk} x^j x^k = k_y h^{\mathrm{TT}}_{jk} x^j x^k = 0
$$
(A.6)

$$
\begin{aligned}
k_k h^{\mathrm{TT}}_{ji} x^j x^k &= k \sin\theta \left(h_{xy} xx + h_{yy} yx + h_{zy} zx \right) \\
&\quad + k \cos\theta \left(h_{xy} xz + h_{yy} yz + h_{zy} zz \right) \\
&= k \sin\theta \left(\frac{h^{(\times)}}{\sqrt{2}} \cos\theta\, xx - \frac{h^{(+)}}{\sqrt{2}} yx - \frac{h^{(\times)}}{\sqrt{2}} \sin\theta\, zx \right) \\
&\quad + k \cos\theta \left(\frac{h^{(\times)}}{\sqrt{2}} \cos\theta\, xz - \frac{h^{(+)}}{\sqrt{2}} yz - \frac{h^{(\times)}}{\sqrt{2}} \sin\theta\, zz \right).
\end{aligned}
$$
(A.7)

Again, the cross terms vanish after averaging. Hence, we obtain

$$
\begin{aligned}
h_{0y} &= \omega_g k \frac{h^{(\times)}}{\sqrt{2}} \cos\theta \sin\theta \left(x^2 - z^2 \right) \left[\frac{\cos(\boldsymbol{k} \cdot \boldsymbol{x})}{(\boldsymbol{k} \cdot \boldsymbol{x})^2} - \frac{\sin(\boldsymbol{k} \cdot \boldsymbol{x})}{(\boldsymbol{k} \cdot \boldsymbol{x})^3} \right] \\
&= \frac{h^{(\times)}}{\sqrt{2}} \cos\theta \sin\theta \left(\tan^2\zeta \cos^2\phi - 1 \right) \\
&\quad \times \left[\cos(kr \cos\zeta) - \frac{\sin(kr \cos\zeta)}{kr \cos\zeta} \right].
\end{aligned}
$$
(A.8)

After the averaging, we have

$$
\langle h_{0y} \rangle = \frac{h^{(\times)}}{\sqrt{2}} \cos\theta \sin\theta\, \bar{F}(\bar{\epsilon}).
$$
(A.9)

Finally, we obtain

$$
\begin{aligned}
\langle \Omega_g \rangle &= \left\langle \boldsymbol{d}^{(34)} \cdot \boldsymbol{E} \right\rangle = d^{(34)i} \varepsilon^{ijk} \langle h^0{}_j \rangle B^k \\
&= d_x^{(34)} \langle h_{0y} \rangle B_z - d_y^{(34)} \langle h_{0x} \rangle B_z \\
&= \frac{B_z}{\sqrt{2}} \sin\theta \left[d_x^{(34)} h^{(\times)} \cos\theta - d_y^{(34)} h^{(+)} \right] \bar{F}(\bar{\epsilon}).
\end{aligned}
$$
(A.10)

Note that $\bar{F}(\bar{\epsilon}) = F(\epsilon)$ and $\bar{\epsilon} = 2\pi\epsilon$.

References

1. B.P. Abbott et al., Observation of gravitational waves from a binary black hole merger. Phys. Rev. Lett. **116**(6), 061102 (2016)
2. B.P. Abbott et al., Prospects for observing and localizing gravitational-wave transients with Advanced LIGO, Advanced Virgo and KAGRA. Living Rev. Relativ. **21**(1), 3 (2018)
3. P. Amaro-Seoane et al., Laser Interferometer Space Antenna (2017)
4. N. Seto, S. Kawamura, T. Nakamura, Possibility of direct measurement of the acceleration of the universe using 0.1-Hz band laser interferometer gravitational wave antenna in space. Phys. Rev. Lett. **87**, 221103 (2001)
5. K. Yagi, N. Seto, Detector configuration of DECIGO/BBO and identification of cosmological neutron-star binaries. Phys. Rev. D **83**, 044011 (2011). [Erratum: Phys. Rev. D **95**, 109901 (2017)]
6. G. Agazie et al., The NANOGrav 15 yr data set: evidence for a gravitational-wave background. Astrophys. J. Lett. **951**(1), L8 (2023)
7. G. Agazie et al., The NANOGrav 15 yr data set: observations and timing of 68 millisecond pulsars. Astrophys. J. Lett. **951**(1), L9 (2023)
8. D.J. Reardon et al., Search for an isotropic gravitational-wave background with the Parkes pulsar timing array. Astrophys. J. Lett. **951**(1), L6 (2023)
9. D.J. Reardon et al., The gravitational-wave background null hypothesis: characterizing noise in millisecond pulsar arrival times with the Parkes pulsar timing array. Astrophys. J. Lett. **951**(1), L7 (2023)
10. A. Zic et al., The Parkes Pulsar Timing Array Third Data Release (2023)
11. J. Antoniadis et al., The second data release from the European Pulsar Timing Array III. Search for gravitational wave signals (2023)
12. J. Antoniadis et al., The second data release from the European Pulsar Timing Array I. The dataset and timing analysis (2023)
13. J. Antoniadis et al., The second data release from the European Pulsar Timing Array: V. Implications for massive black holes, dark matter and the early Universe (2023)
14. X. Heng et al., Searching for the nano-hertz stochastic gravitational wave background with the Chinese pulsar timing array data release I. Res. Astron. Astrophys. **23**(7), 075024 (2023)
15. K. Saito, J. Soda, H. Yoshino, Universal 1020 Hz stochastic gravitational waves from photon spheres of black holes. Phys. Rev. D **104**(6), 063040 (2021)
16. A. Ito, K. Kohri, K. Nakayama, Probing high frequency gravitational waves with pulsars (2023)
17. A. Ito, J. Soda, MHz gravitational waves from short-term anisotropic inflation. JCAP **04**, 035 (2016)
18. A. Ito, J. Soda, M. Yamaguchi, Analytic formula for the dynamics around inflation end and implications on primordial gravitational waves. JCAP **03**, 033 (2021)
19. C. Caprini, D.G. Figueroa, Cosmological backgrounds of gravitational waves. Class. Quantum Gravity **35**(16), 163001 (2018)
20. C. Clarkson, S.S. Seahra, A gravitational wave window on extra dimensions. Class. Quantum Gravity **24**, F33–F40 (2007)
21. N. Aggarwal et al., Challenges and opportunities of gravitational-wave searches at MHz to GHz frequencies. Living Rev. Relativ. **24**(1), 4 (2021)
22. T. Akutsu et al., Search for a stochastic background of 100-MHz gravitational waves with laser interferometers. Phys. Rev. Lett. **101**, 101101 (2008)
23. A. Ito, T. Ikeda, K. Miuchi, J. Soda, Probing GHz gravitational waves with graviton–magnon resonance. Eur. Phys. J. C **80**(3), 179 (2020)
24. A. Ito, J. Soda, A formalism for magnon gravitational wave detectors. Eur. Phys. J. C **80**(6), 545 (2020)

25. A. Ejlli, D. Ejlli, A.M. Cruise, G. Pisano, H. Grote, Upper limits on the amplitude of ultra-high-frequency gravitational waves from graviton to photon conversion. Eur. Phys. J. C **79**(12), 1032 (2019)

26. V. Domcke, C. Garcia-Cely, N.L. Rodd, Novel search for high-frequency gravitational waves with low-mass axion haloscopes. Phys. Rev. Lett. **129**(4), 041101 (2022)

27. G. Engelhardt, A. Bhoonah, W. Vincent Liu, Detecting axion dark matter with Rydberg atoms via induced electric dipole transitions (2023)

28. T.F. Gallagher, Rydberg atoms, in *Springer Handbook of Atomic, Molecular, and Optical Physics* (Springer, 1994), pp. 231–240

29. C.L. Degen, F. Reinhard, P. Cappellaro, Quantum sensing. Rev. Mod. Phys. **89**(3), 035002 (2017)

30. Y.-Y. Jau, T. Carter, Vapor-cell-based atomic electrometry for detection frequencies below 1 khz. Phys. Rev. Appl. **13**(5), 054034 (2020)

31. C.G. Wade, N. Šibalić, N.R. de Melo, J.M. Kondo, C.S. Adams, K.J. Weatherill, Real-time near-field terahertz imaging with atomic optical fluorescence. Nat. Photonics **11**(1), 40–43 (2017)

32. L.A. Downes, A.R. MacKellar, D.J. Whiting, C. Bourgenot, C.S. Adams, K.J. Weatherill, Full-field terahertz imaging at kilohertz frame rates using atomic vapor. Phys. Rev. X **10**(1), 011027 (2020)

33. M. Jing, H. Ying, J. Ma, H. Zhang, L. Zhang, L. Xiao, S. Jia, Atomic superheterodyne receiver based on microwave-dressed Rydberg spectroscopy. Nat. Phys. **16**(9), 911–915 (2020)

34. U. Fischer, Transition probabilities for a Rydberg atom in the field of a gravitational wave. Class. Quantum Gravity **11**(2), 463 (1994)

35. M.O. Scully, M. Suhail Zubairy, Quantum optics (1999)

36. T. Autler, Stark effect in rapidly varying fields. Phys. Rev. D **100**, 703–722 (1955)

37. M. Fleischhauer, A. Imamoglu, J.P. Marangos, Electromagnetically induced transparency: optics in coherent media. Rev. Mod. Phys. **77**, 633–673 (2005)

38. P.L. Fortini, C. Gualdi, Fermi normal co-ordinate system and electromagnetic detectors of gravitational waves. I. Calculation of the metric. Nuovo Cimento B Ser. **71**, 37–54 (1982)

39. K.-P. Marzlin, Fermi coordinates for weak gravitational fields. Phys. Rev. D **50**, 888–891 (1994)

40. M. Rakhmanov, Fermi-normal, optical, and wave-synchronous coordinates for spacetime with a plane gravitational wave. Class. Quantum Gravity **31**, 085006 (2014)

41. A. Berlin, D. Blas, R.T. D'Agnolo, S.A.R. Ellis, R. Harnik, Y. Kahn, J. Schütte-Engel, Detecting high-frequency gravitational waves with microwave cavities. Phys. Rev. D **105**(11), 116011 (2022)

42. A. Ito, J. Soda, Exploring High Frequency Gravitational Waves with Magnons (2022)

43. E.J. Robertson, N. Šibalić, R.M. Potvliege, M.P.A. Jones, Arc 3.0: an expanded python toolbox for atomic physics calculations. Comput. Phys. Commun. **261**, 107814 (2021)

44. J.P. Harald Kübler, T.B. Shaffer, R. Löw, T. Pfau, Coherent excitation of Rydberg atoms in micrometre-sized atomic vapour cells. Nat. Photonics **4**(2), 112–116 (2010)

45. H. Fan, S. Kumar, J. Sedlacek, H. Kübler, S. Karimkashi, J.P. Shaffer, Atom based rf electric field sensing. J. Phys. B At. Mol. Opt. Phys. **48**(20), 202001 (2015)

46. D.H. Meyer, Z.A. Castillo, K.C. Cox, P.D. Kunz, Assessment of Rydberg atoms for wideband electric field sensing. J. Phys. B At. Mol. Opt. Phys. **53**(3), 034001 (2020)

47. M. Goryachev, D.L. Creedon, S. Galliou, M.E. Tobar, Observation of Rayleigh phonon scattering through excitation of extremely high overtones<? format?> in low-loss cryogenic acoustic cavities for hybrid quantum systems. Phys. Rev. Lett. **111**(8), 085502 (2013)

48. S. Galliou, M. Goryachev, R. Bourquin, P. Abbé, J.P. Aubry, M.E. Tobar, Extremely low loss phonon-trapping cryogenic acoustic cavities for future physical experiments. Sci. Rep. **3**(1), 2132 (2013)

49. C. Bartram et al., Search for invisible axion dark matter in the 3.3–4.2 μeV mass range. Phys. Rev. Lett. **127**(26), 261803 (2021)

50. K. Schmieden, M. Schott, A global network of cavities to search for gravitational waves (GravNet): a novel scheme to hunt gravitational waves signatures from the early universe. PoS, **EPS-HEP2023**, 102 (2024)

51. D.J. Fixsen et al., ARCADE 2 measurement of the extra-galactic sky temperature at 3–90 GHz. Astrophys. J. **734**, 5 (2011)

52. A. Ringwald, J. Schütte-Engel, C. Tamarit, Gravitational waves as a big bang thermometer. JCAP **03**, 054 (2021)

53. F.-Y. Li, M.-X. Tang, D.-P. Shi, Electromagnetic response of a gaussian beam to high-frequency relic gravitational waves in quintessential inflationary models. Phys. Rev. D **67**(10), 104008 (2003)

54. G. Franciolini, A. Maharana, F. Muia, Hunt for light primordial black hole dark matter with ultrahigh-frequency gravitational waves. Phys. Rev. D **106**(10), 103520 (2022)